https://dx.doi.org/10.1016/j.chemosphere.2018.04.090



# Maximization of Current Efficiency for Organic pollutants Oxidation at BDD, Ti/$SnO_2$-Sb/$PbO_2$, and Ti/$SnO_2$-Sb Anodes

Xuan Xing[a], Jinren Ni[b*],Xiuping Zhu[c], Yi Jiang[d], Jianxin Xia[a]

[a] College of Life and Environmental Science, Minzu University of China, Beijing 100081, China

[b] Department of Environmental Engineering, Peking University, the Key Laboratory of Water and Sediment Sciences, Ministry of Education, Beijing100871, China

[c] Department of Civil and Environmental Engineering, Louisiana State University, Baton Rouge, Louisiana 70803, United States

[d] Department of Civil and Environmental Engineering, The Hong Kong Polytechnic University, Hung Hom, Kowloon, Hong Kong

[*]Corresponding author. Tel.: +86 10 6275 1185; fax: +86 10 6275 6526.

*E-mail address:* nijinren@iee.pku.edu.cn (J.R. Ni).

## Abstract

Whereas electrochemical oxidation is noted for its ability to degrade bio-refractory organics, it has also been incorrectly criticized for excessive energy consumption. The present paper rectifies this misunderstanding by demonstrating that the energy actually consumed in the degradation process is much less than that wasted in the side reaction of oxygen evolution. To minimize the side reaction, the possible highest instantaneous current efficiency (PHICE) for electrochemical oxidation of phenol at Boron-doped Diamond (BDD), Ti/$SnO_2$-Sb/$PbO_2$ ($PbO_2$), and Ti/$SnO_2$-Sb ($SnO_2$) anodes has been investigated systematically, and found to reach almost 100% at the BDD anode compared with 23% at the $PbO_2$ anode and 9% at the $SnO_2$ anode. The significant discrepancy between PHICE values at the various anodes is interpreted in terms of different existing forms of hydroxyl radicals. For each anode system, the PHICEs are maintained experimentally using a computer-controlled exponential decay current mode throughout the electrolysis process. For applications, the minimized energy consumption is predicted by response surface methodology (RSM), and demonstrated for the BDD anode system. Consequently, almost 100% current efficiency is achieved (for a relatively meagre energy consumption of 17.2 kWh $kgCOD^{-1}$) along with excellent COD degradation efficiency by optimizing the initial current density, flow rate, electrolysis time, and exponential decay constant. Compared with galvanostatic conditions, over 70% of the energy is saved in the present study, thus demonstrating the great potential of electrochemical oxidation for practical applications.

**Key words:** Possible highest instantaneous current efficiency, Exponential decay current mode, Electrochemical oxidation, Energy Saving, Response surface methodology.

## 1. Introduction

Many industrial processes generate bio-refractory organic effluent, such as coking processes (Lai et al. 2009; Zhu et al. 2009), oil refining(Wei et al. 2010), textile dyeing(Abdessamad et al. 2013; Sathishkumar et al. 2017), the production of pharmaceutics (Wang et al. 2017), pesticide (Wee and Aris 2017), herbicide (Allan et al. 2017), pulp and paper (Fang et al. 2017), plastics and detergents (Hermabessiere et al. 2017). Such wastewaters usually contain many kinds of bio-refractory organic compounds, and so cannot be degraded efficiently by conventional biological methods. Instead, advanced oxidation processes (AOPs) including Fenton oxidation (Gupta and Garg 2018), ozonation (Chacana et al. 2017), wet air oxidation (Li et al. 2013), photocatalytic oxidation (Uyguner-Demirel and Bekbolet 2011), supercritical water oxidation (Yang et al. 2017) and electrochemical oxidation (Zhu et al. 2009; Zhu and Ni 2011; Yi et al. 2010; Xing et al. 2012; Li et al. 2010) have been widely investigated to treat these wastewaters.

Electrochemical oxidation is one of the most promising AOPs techniques because of its low use of chemicals, fast oxidization rate, and lack of secondary pollution. However, the electrochemical oxidation method has long been criticized for its poor current efficiency (CE) and high energy consumption, and so has not been widely applied. To remedy these defects, a considerable body of research has been undertaken on combinations of various oxidation methods (Cañizares et al. 2009; Garcia-Segura et al. 2012; Borràs et al. 2011; Brillas et al. 2004) and the enhancement of mass transfer processes (Lindermeir et al. 2003; Zhao et al. 2008). However, many

problems persist such as the need of extra chemicals, dependence on specialized equipment, formation of complex substances, etc., and no satisfactory results have been obtained to date.

Anode materials are critical for electrochemical oxidation processes and have a significant influence on CE. Over the past few decades, various anodes have been tested including Pt (Zhao et al. 2008), $IrO_2$ (Martínez-Huitle et al. 2004), $RuO_2$ (Zhou et al. 2011), $PbO_2$ (He et al. 2018), $SnO_2$ (Guo et al. 2016), and boron-doped diamond (BDD) anodes (Panizza and Cerisola 2005; Li et al. 2010; Zhu et al. 2011b; Zhu et al. 2010a; Wei et al. 2011). According to the oxidation mechanism, these anodes can be divided into two groups, i.e. active anodes and non-active anodes (Zhu et al. 2008; Zhu et al. 2007). During electrolysis, water molecules initially oxidize on the anode surface ($MO_x$) leading to the formation of hydroxyl radicals ($MO_x(\bullet OH)$). At active anodes, such as Pt, $IrO_2$ and $RuO_2$, the hydroxyl radicals oxidize the oxide lattice and form higher oxides ($MO_{x+1}$) that participate in the electrochemical conversion of organic pollutants. At non-active anodes, such as $SnO_2$, $PbO_2$ and BDD, the hydroxyl radicals are mainly physically adsorbed and react with organics directly. Besides oxidizing organics, oxygen is evolved through further oxidation of the hydroxyl radicals. This decomposition process wastes energy during electrolysis and this worsens the longer the duration of the process. Hence, it can be speculated that if the side reaction of oxygen evolution can be prevented or minimized, then energy consumption would be substantially reduced. Recently, a multi-step modulation method involving complicated adjustment to the applied current has been proposed

(Panizza et al. 2008) to enhance CE in a BDD anode system. Simplification of this method would make it attractive for use in practical applications.

In the present study, the possible highest instantaneous current efficiency (PHICE) of three typical systems with non-active anodes of BDD, Ti/$SnO_2$-Sb/$PbO_2$ ($PbO_2$), and Ti/$SnO_2$-Sb ($SnO_2$) is investigated by reducing the side reaction. Using a computer-controlled exponential decay current mode, the PHICE is successfully maintained throughout the electrolysis process without being affected by the electrolysis time. System optimization using response surface methodology (RSM) is conveniently undertaken by altering the following operating parameters: initial current density, electrolysis time, flow rate, and exponential decay constant *k*. The optimization technique is demonstrated for phenol (Wei et al. 2011; Zhu and Ni 2011; Yi et al. 2010) electrochemical oxidation in a BDD anode system.

## 2. Experimental Section

### 2.1 Electrochemical system

A diagram illustrating the electrochemical installation is given in Figure S1, which is constant with previous study (Zhu et al. 2010b). The three anodes respectively comprise BDD (purchased from CONDIAS GmbH, Germany), $PbO_2$ and $SnO_2$ electrodes (purchased from the General Research Institute for Nonferrous Metals, Beijing, China), each with a working area of 24 $cm^2$ (3 × 8 cm). A piece of stainless steel of the same dimensions is used as the cathode. The gap between the electrodes is set to be 1.55 cm, and thus the working volume of the system is 37.2 mL. The anode system is operated in continuous mode at room temperature for phenol

simulated wastewater. During the electrochemical oxidation process, the water contaminated with phenol is pumped from a tank at a constant flow rate through the reactor. At regular intervals, samples are drawn from the tank for chemical analysis.

**2.2 Analytical methods**

Phenol concentration is measured by an Agilent HP1100 HPLC instrument with a ZORBAX SB-$C^{18}$ column and a DAD detector. The UV detector is set at 217 nm for phenol detection. The mobile phase is methanol: water (50:50), with a constant flow rate of 1.0 mL $min^{-1}$. Initial chemical oxygen demand (COD) of the phenol simulated wastewater is controlled at 500 mg $L^{-1}$ with 0.1 M $Na_2SO_4$ as the electrolyte. COD is measured by a titrimetric method using dichromate as the oxidant in an acidic solution at 150°C for 2 h (Hachi, USA). The instantaneous current efficiency (*ICE*) for the anodic oxidation of phenol is determined from:

$$ICE = \frac{[COD_t - COD_{\Delta t}]\mathrm{F}V}{8I\Delta t} \qquad (1)$$

where $COD_t$ and $COD_{t+\triangle t}$ are the COD (g $O_2$ $m^{-3}$) at times $t$ and $t+\triangle t$ (s), respectively. F is the Faraday constant (96,487 C $mol^{-1}$), $V$ is the volume of the electrolyte (L), $I$ is the current (in A), and the number 8 is a dimensional factor for consistency of units (32 g $O_2$/4 mol $e^{-1}$ $O_2$).

The time-averaged current efficiency (*CE*) is calculated using the mean-value theorem from:

$$CE = \frac{\int_0^{\tau} ICE(t)dt}{\tau} \qquad (2)$$

where τ is the electrolysis duration (s) necessary to reach a target COD conversion.

129 Degradation efficiency ($D_{COD}$) is calculated using:

$$D_{COD} = \frac{COD_0 - COD_t}{COD_0} \times 100\% \quad (3)$$

130

131 where $COD_0$ is the initial concentration, $COD_t$ is the concentration after electrolysis

132 time t (h).

133 The specific energy consumption per unit mass of COD ($E_{sp}$, kWh $kgCOD^{-1}$) is

134 calculated from:

$$E_{sp} = \frac{1000UIt}{(COD_{in} - COD_{out})V} \quad (4)$$

135

136 where $U$ is the cell voltage (V), $I$ is the current (A), $t$ is the electrolysis time (h),

137 $COD_{in}$ and $COD_{out}$ are the influent and effluent COD of wastewater (mg $L^{-1}$) and $V$ is

138 the reactor volume (L).

139 **2.3 Detection of hydroxyl radicals**

140 N,N-dimethy-*p*-nitrosoaniline (RNO) is used as a spin trap of hydroxyl radicals

141 according to the reference (Comninellis 1994). The change of the yellow color of

142 RNO is measured by UV-vis spectrophotometer (Specord 200, Analytikjena) at 440

143 nm. Electrolysis is performed in a 250 mL phosphate buffer (pH 7.1) solution

144 containing $3\times10^{-5}$ M RNO at room temperature of 25 ℃ for 60 min. BDD, $PbO_2$ and

145 $SnO_2$ (4 $cm^{-2}$) electrodes are used as anode respectively with stainless steel used as

146 cathode. The gap between electrodes is set as 10 mm and the solution is stirred by a

147 magnetic stirring bar.

148 **2.4 Exponential decay current mode**

149 The power supply (DH1765-1), provided by Beijing Dahua Electron Co. Ltd.,

China, is computer-controlled through adjustments to two operating parameters: the initial current density ($i_{lim}$) and the exponential decay constant $k$. The current density is kept constant after decaying to 5 mA $cm^{-2}$ in order to ensure that the reaction occurs in the region of water decomposition (Panizza and Cerisola 2005; Panizza et al. 2008).

**2.5 Response surface methodology**

Response surface methodology (RSM) is used to optimize the experimental conditions and to analyze the influence of operating parameters on the electrochemical oxidation of phenol in the exponential decay current mode. Second-order central composite design (CCD) is employed to determine the combinations of input parameters used in the test program.

The initial current density ($X_1$), flow rate ($X_2$), electrolysis time ($X_3$) and exponential decay constant $k$ ($X_4$), all of which have significant influence on electrochemical oxidation processes, are chosen as independent variables. The degradation efficiency ($D_{COD}$) and specific energy consumption ($E_{sp}$) are chosen as output variables. Table 1 lists the independent variables and their experimental ranges. For statistical calculations, the variables $X_i$ are coded in normalized form as $x_i \in [-2, 2]$ according to:

$$x_i = \frac{X_i - X_0}{\delta X} \qquad (5)$$

where $X_0$ is the value of $X_i$ at the center point and $\delta X$ represents the step change.

Experimental data are analyzed using response surface regression by means of the software package Minitab 16 and fitting to the second-order polynomial model:

$$Y=b_0 + b_1x_1 + b_2x_2 + b_3x_3 + b_4x_4 + b_{11}x_1^2 + b_{22}x_2^2 + b_{33}x_3^2 + b_{44}x_4^2$$

$$+b_{12}x_1x_2 + b_{13}x_1x_3 + b_{14}x_1x_4 + b_{23}x_2x_3 + b_{24}x_2x_4 + b_{34}x_3x_4 \qquad (6)$$

where $Y$ is the response variable, $b_0$ is a constant; $b_1$, $b_2$, $b_3$ and $b_4$ are regression coefficients for linear effects; $b_{11}$, $b_{22}$, $b_{33}$ and $b_{44}$ are quadratic coefficients; and $b_{12}$,$b_{13}$,$b_{14}$, $b_{23}$, $b_{24}$ and $b_{34}$ are interaction coefficients.

## 3. Results and discussion

### 3.1 PHICE at different anodes

According to previous studies (Zhu et al. 2008; Zhu et al. 2007), the side reaction of oxygen evolution is the primary cause for energy waste at non-active anodes. Hence, minimization of the side reaction is the key factor in energy saving. Here, a theoretical model is proposed by which to predict the limiting current density of BDD anode, assuming that oxidation process is controlled by diffusion (Panizza et al. 2001). Using this model, the limiting current density is estimated from the COD concentration:

$$i_{\lim}(t) = 4\mathrm{F}k_{\mathrm{m}}\, COD(t) \qquad (7)$$

where $i_{\lim}$ is the limiting current density (A $m^{-2}$) at a given time $t$, 4 is the number of exchange electrons per mol of $O_2$, F is the Faraday constant (C $mol^{-1}$), $k_m$ is the average mass transport coefficient in the electrochemical reactor (m $s^{-1}$), and $COD(t)$ is the chemical oxygen demand (mol $O_2$ $m^{-3}$) at a given time $t$.

Rates of reaction between the organics and hydroxyl radicals were different at the three non-active BDD, $PbO_2$ and $SnO_2$ electrodes because of the various forms of hydroxyl radicals encountered. At the BDD anode, the hydroxyl radicals were weakly

adsorbed and tended to exist freely in a region near the anode surface. As a result, the hydroxyl radicals reacted vigorously with the organics, and were utilized efficiently in the oxidation process (Panizza and Cerisola 2004; Zhu et al. 2009; Zhu et al. 2008). On the contrary, at $PbO_2$ and $SnO_2$ anodes, the hydroxyl radicals were strongly adsorbed at the anode surface and hence were readily wasted in the side reaction of oxygen evolution (Figure S2). Thus, the limiting current density for $PbO_2$ and $SnO_2$ anodes cannot be determined from the COD concentration, unlike for the BDD anode. Meanwhile different existing forms of hydroxyl radicals have been analyzed using a mathematical model based on van der Waals interaction (Vatistas 2010). In this model, the solution adjacent to the anode surface is divided into different layers (Figure S3). The layer nearest the anode surface is defined as the adsorption layer and is taken to be the region in which oxygen forms. Most of the hydroxyl radicals are assumed to be located in the adsorption layer and only those which can diffuse out of the layer are able to react with organic pollutants efficiently. The thickness of the adsorption layer $\delta$ depends on the anode material properties and exercises considerable influence on their ICE. At the BDD anode, $\delta$ is almost zero, and consequently all generated hydroxyl radicals can be utilized in the oxidation process. However, at the $PbO_2$ and $SnO_2$ anodes, the majority of generated hydroxyl radicals remains trapped in the adsorption layer and is utilized wastefully in the side reaction.

In order to estimate the utilization efficiency of hydroxyl radicals produced at the $PbO_2$ and $SnO_2$ anodes, the ICE was estimated under certain experimental conditions consistent with those for the limiting current density investigation at the BDD anode.

For conditions of initial COD of 500 mg $L^{-1}$, flow rate of 250 mL $min^{-1}$, mass-transfer coefficient $k_m$ of $1.8\times10^{-5}$ m $s^{-1}$ (determined using the ferri/ferrocyanide couple), and supporting electrolyte 0.1 M of $Na_2SO_4$, the limiting current density $i_{lim}$ was 11 mA $cm^{-2}$ (calculated using Eq. 7). Under these conditions, almost 100% ICE was achieved in the BDD anode system, implying that electrons supplied by the power source met exactly the COD degradation requirement. These results demonstrated the excellent catalytic capability of the BDD anode to convert electronic energy to chemical energy. However, under the same experimental conditions, the values of ICE were only 23% and 9% at the $PbO_2$ and $SnO_2$ anodes, indicating that 77% and 91% hydroxyl radicals were wasted in the side reaction. For the limiting experimental conditions, these ICE values can be identified as the corresponding PHICE values at the three non-active anodes considered here for phenol oxidation.

### 3.2 Exponential decay current mode for PHICE

Under galvanostatic conditions, the time-averaged current efficiency (CE) (calculated using Eq. 2) decreased with electrolysis time $\tau$ due to the growing side reaction of oxygen evolution (Jiang et al. 2010; Xing et al. 2012; Zhu et al. 2007). In order to maintain the idealized ICE throughout the entire electrolysis process and remove any influence of electrolysis time, a specially designed exponential decay current mode was applied to the electrolysis process. In this mode of operation, the current was instantaneously adjusted using control software to remain at the limiting value (calculated using Eq. 6). Consequently, CE was able to achieve the maximum value without being affected by the electrolysis time $\tau$.

238 This above current mode was applied to each of the three non-active anode
239 systems using operating parameters consistent with the experimental conditions in
240 Section 3.1. Under galvanostatic conditions with current density of 11 mA $cm^{-2}$, the
241 observed COD removal followed an exponential trend given by:

242 $$COD_t = COD_0 \times \exp(-k_{COD} t) \quad (8)$$

243 The exponential decay constant $k$ in the current mode was set to be the same as
244 $k_{COD}$ which had values of $8\times10^{-5}$, $2\times10^{-5}$ and $7\times10^{-6}$ $s^{-1}$ respectively for the BDD, $PbO_2$,
245 and $SnO_2$ anodes. Figure 1 presents the results for electrochemical oxidation of
246 phenol at the three anodes obtained using the exponential decay current mode. The
247 figure shows the degradation of phenol (A), removal percentage of COD (B),
248 intermediate concentration (C) and CE (D) as functions of time during the entire
249 electrolysis process for the BDD, $PbO_2$ and $SnO_2$ anodes, respectively. It may easily
250 be seen that the degradation rate of phenol at the BDD anode was much faster than at
251 the $PbO_2$ and $SnO_2$ anodes. After 3 h electrolysis, the COD removal percentage was
252 69.2% at BDD anode, a much higher value than the 17.6% and 7% obtained for the
253 $PbO_2$ and $SnO_2$ anodes. Here, COD represents the total concentration of organic
254 compounds in solution, including phenol and all the intermediates formed during the
255 electrolysis process. Hence, the subtracted difference between the percentage of
256 phenol and the COD indicates the presence of intermediates formed at the three
257 anodes. The least amount of intermediates was produced at the $SnO_2$ anode because of
258 the slow removal rates of both phenol and COD. The most intermediates were
259 produced at $PbO_2$ anode owing to the much faster degradation rate of phenol than its

mineralization at the $PbO_2$ anode. Intermediates did not accumulate too much in the BDD anode system due to its fast removal rates of both phenol and COD, in accordance with the excellent mineralization ability of the BDD anode. CE usually decayed rapidly with electrolysis time under galvanostatic conditions, but remained constant for each of the three anodes during the entire process when the computer-controlled exponential decay current mode was applied. Throughout the electrolysis process, the PHICE was maintained at each of the BDD, $PbO_2$ and $SnO_2$ anodes under consideration. Correspondingly, the specific energy consumption for per unit mass COD, $E_{sp}$, was lowest at 17.6 kWh $kgCOD^{-1}$ for the BDD anode, and much higher at 62.6 and 170.2 kWh $kgCOD^{-1}$ for the $PbO_2$ and $SnO_2$ anodes.

Quantity of hydroxyl radicals formed during electrolysis process under exponential decay current mode at the three non-active anodes has been examined by RNO (Figure 2A), respectively. The experimental conditions were the same with COD degradation at the three anode materials. Referred previous study (Zhao et al. 2010), the index of $\Delta COD/[\bullet OH]_{total}$ has been introduced to describe the utilization of hydroxyl radicals. According to the experimental results (Figure 2B), it is obviously that the value of $\Delta COD/[\bullet OH]_{total}$ for BDD anode at 60 min was 169.2, which was the highest, and 31.2, 17.4 for $PbO_2$ and $SnO_2$, respectively. In order to compare these values intuitively, the value on BDD was taken as 100%, which was constant with its PHICE, so those on $PbO_2$ and $SnO_2$ anode were 20.5% and 11.8%. It has been reported that oxidation at non-active anodes was meanly due to indirect oxidation by free hydroxyl radicals, therefore the utilization efficiency can be

identified as the percentage of free hydroxyl radicals existing at these anode surface.

### 3.3 RSM analysis for PHICE in BDD anode system

The preceding results have shown that the ideal ICE can be maintained throughout the entire electrolysis process in three non-active anode systems using a computer-controlled exponential decay current mode. In order to gain a deeper understanding of this mode, the influence of and interactions between its parameters have been interpreted using RSM analysis of the BDD anode system. Table 1 lists the design matrix obtained from full factor central composite design (CCD) and used for experimental test cases on the electrochemical oxidation of phenol simulated wastewater investigated in the BDD anode system. Table 2 lists the values of $D_{COD}$ and $E_{sp}$ obtained for each case. For the various operating conditions, the value of $D_{COD}$ was in the range 20.04 ~ 71.03% and that of $E_{sp}$ was in the range 16.3 ~ 24.92 kWh $kgCOD^{-1}$.

The experimental data are analyzed using the response surface regression procedures in RSM and fitted to a second-order polynomial model (Eq. 5). The regression curves obtained for the response variable $Y$ related to $D_{COD}$ and $E_{sp}$ are as follows:

$$Y(D_{COD}) = 50.96 + 8.408x_1 + 5.895x_2 + 24.873x_3 - 2.41x_4 - 3.053x_1^2 - 4.343x_2^2 - 7.513x_3^2 - 1.267x_4^2 + 4.61x_1x_2 + 7.325x_1x_3 - 4.165x_1x_4 - 3.195x_2x_3 - 5.035x_2x_4 - 5.44x_3x_4 \quad (R^2 = 0.9556) \quad (9)$$

$$Y(E_{sp}) = 18.9571 + 3.8792x_1 - 2.0742x_2 - 0.7642x_3 - 0.4075x_4 + 1.3283x_1^2 + 2.4783x_2^2 + 0.4933x_3^2 - 1.0117x_4^2 - 2.0625x_1x_2 - 2.7275x_1x_3 + 2.4675x_1x_4 - 1.2875x_2x_3$$

$$+ 0.0575x_2x_4 + 0.3925x_3x_4 \qquad (R^2 = 0.9377) \qquad (10)$$

where $x_1$ is the normalized initial current density, $x_2$ is the normalized flow rate, $x_3$ is the normalized electrolysis time, and $x_4$ is the normalized exponential decay constant. The correlation coefficients ($R^2$) listed alongside Eq. 9 and Eq. 10 are high. Figure 3A and Figure 3B confirm that excellent agreement is obtained between the experimental and predicted values of $D_{COD}$ and $E_{sp}$ in all cases. We now consider the residuals in order to examine deviations between the experimental and the predicted results. The error terms are assumed to be random and therefore normally distributed about zero mean with constant standard deviation. Figure 3C and Figure 3D plot the normalized probability against the residuals of $D_{COD}$ and $E_{sp}$. In both subplots, the points or point clusters are located close to the diagonal line. From this it may be concluded that it was reasonable to assume that the errors were normally distributed and independent of each other. The homogeneity of the error variances and independence of the residuals demonstrate that the RSM model (Eq. 9 and Eq. 10) is appropriate for describing both $D_{COD}$ and $E_{sp}$ in the electrochemical oxidation process considered herein.

In the electrochemical oxidation process using the BDD anode system, both COD degradation efficiency ($D_{COD}$) and specific energy consumption per unit mass of COD ($E_{sp}$) were significantly affected by the ambient operating conditions. Figure 4 and Figure 5 present contour plots of $D_{COD}$ and $E_{sp}$ obtained for different combinations of primary factors; namely, the initial current density *i*, flow rate *v*, electrolysis time *t* and exponential decay constant *k*.

Pairwise comparisons of the four influence factors affecting $D_{COD}$ demonstrated

326 that electrolysis time was the most significant factor, when compared against either
327 initial current density (Figure 4B) or flow rate (Figure 4C) or exponential decay
328 constant *k* (Figure 4D). However, the initial current density and flow rate exhibit
329 similar extents of influence (Figure 4A). Taking into account all the results, the
330 overall influence order of the factors on $D_{COD}$ was $t > i > v > k$. This suggests that to
331 obtain higher degradation efficiency requires longer electrolysis time, higher initial
332 current density, faster flow rate, and smaller exponential decay constant *k*.

333 Turning to $E_{sp}$, the initial current density was more significant than the flow rate
334 (Figure 5A), electrolysis time (Figure 5B) or decay constant *k* (Figure 5D). The flow
335 rate was more important than electrolysis time (Figure 5B). Thus, the influence order
336 of the factors on $E_{sp}$ was $i > v > t > k$, implying that lower energy consumption
337 requires lower initial current density, faster flow rate, and longer electrolysis time.

338 Surprisingly, the relationship between $E_{sp}$ and electrolysis time under the
339 exponential decay current mode does not follow the general understanding reported
340 previously (Zhu et al. 2007). Under the computer-controlled exponential decay
341 current mode, $E_{sp}$ tended to decrease with increasing electrolysis time, unlike cases
342 operated under galvanostatic conditions. Besides COD concentration and current
343 density, $E_{sp}$ is also influenced by the cell voltage U (Eq. 4). The cell voltage is
344 particularly high during the initial stage of electrolysis and later decreases with time
345 when the system is operated under the exponential decay current mode. By combining
346 Eqs.1,2 and 4, $E_{sp}$ can be expressed as:

347
$$E_{sp} = 125\mathrm{F}\frac{U}{CE} \qquad (11)$$

348 in which *CE* is taken as constant under exponential decay current mode, so that $E_{sp}$
349 declines with *U* over the duration of the electrolysis process.

350 It should be stressed that both $D_{COD}$ and $E_{sp}$ would be enhanced by lengthening
351 the electrolysis time under the exponential decay current mode which overcomes the
352 difficulties encountered under conventional galvanostatic conditions (Panizza and
353 Cerisola 2004; Zhu et al. 2007; Yi et al. 2010; Xing et al. 2012). This breakthrough
354 should lead to major benefits in the application of electrochemical oxidation systems
355 that involve considerably less energy consumption.

356 To examine these findings, the following example concerns the optimized
357 condition in a BDD anode system obtained using the RSM model, for given operating
358 conditions of $i$ =11.53 mA $cm^{-2}$, $v$ = 253 mL $min^{-1}$, $t$ = 180 min and $k = 6\times10^{-5}$ $s^{-1}$. For
359 the phenol simulated wastewater, over 70% COD was removed from the initial 500
360 mg $L^{-1}$ phenol content (the remainder having COD < 150 mg $L^{-1}$ as required by the
361 National Discharge Standard of China) within 3 h with an $E_{sp}$ value of merely 17.2
362 kWh $kgCOD^{-1}$. For comparison, the RSM-minimized value of $E_{sp}$ under galvanostatic
363 conditions was 63 kWh $kgCOD^{-1}$ when operated under continuous mode (Zhu et al.
364 2010b) and 84.79 kWh kg $COD^{-1}$ under batch mode (Zhu et al. 2011a). Moreover, the
365 energy saving through other modes, e.g. the pulse current mode (Wei et al. 2011), was
366 not as encouraging as that from the exponential decay mode proposed in the present
367 paper.

## 4. Conclusion

In summary, PHICE has been achieved for three non-active anode systems by reducing the side reaction to its lowest level and maintaining this throughout the whole electrolysis period using a computer-controlled exponential decay current mode. A demonstration case of electrochemical oxidation of phenol by the exponential decay current mode for the BDD anode system was analyzed by RSM. These results showed almost 100% CE was achieved, with $E_{sp}$ of merely 17.2 kWh kg $COD^{-1}$, along with excellent COD degradation efficiency. Meanwhile, $D_{COD}$ enhancement and $E_{sp}$ reduction occurred simultaneously as the electrolysis time increased, which never happens under conventional galvanostatic conditions. Systematic analysis of experimental results under comparable conditions indicated that about 73% energy that would otherwise be wasted in the side reaction could be retrieved by exerting an exponential decay current mode in the BDD anode system. This huge gain in energy has corrected a long-held misunderstanding that the BDD anode system is energy inefficient when degrading bio-refractory organics, and points towards the potential of electrochemical oxidation method for practical applications.

## Acknowledgement

This work was supported by Natural Science Foundation of China. (No. 51409285).

389 **References**

390 Abdessamad, N., Akrout, H., Hamdaoui, G., Elghniji, K., Ksibi, M., and Bousselmi,
391 L., 2013. Evaluation of the efficiency of monopolar and bipolar BDD
392 electrodes for electrochemical oxidation of anthraquinone textile synthetic
393 effluent for reuse. Chemosphere 93, 1309-1316.
394 Allan, H. L., Van, J. P., Finlayson, K. A., O'Brien, J. W., Mueller, J. F., and Leusch, F.
395 D. L., 2017. Analysis of sugarcane herbicides in marine turtle nesting areas
396 and assessment of risk using in vitro toxicity assays. Chemosphere
397 185,656-664.
398 Borràs, N., Arias, C., Oliver, R., and Brillas, E., 2011. Mineralization of desmetryne
399 by electrochemical advanced oxidation processes using a boron-doped
400 diamond anode and an oxygen-diffusion cathode. Chemosphere 85,1167-1175.
401 Brillas, E., Boye, B., Sirés, I., Garrido, J. A., Rodríguez, R. M. a., Arias, C., Cabot,
402 P.-L., and Comninellis, C., 2004. Electrochemical destruction of
403 chlorophenoxy herbicides by anodic oxidation and electro-Fenton using a
404 boron-doped diamond electrode. Electrochim. Acta 49, 4487-4496.
405 Cañizares, P., Paz, R., Sáez, C., and Rodrigo, M. A., 2009. Costs of the
406 electrochemical oxidation of wastewaters: A comparison with ozonation and
407 Fenton oxidation processes. J. Environ. Manage. 90, 410-420.
408 Chacana, J., Alizadeh, S., Labelle, M.-A., Laporte, A., Hawari, J., Barbeau, B., and
409 Comeau, Y., 2017. Effect of ozonation on anaerobic digestion sludge activity
410 and viability. Chemosphere 176, 405-411.

411 Comninellis, C. 1994. Electrocatalysis in the electrochemical conversion/combustion
412 of organic pollutants for waste water treatment. Electrochim. Acta 39,
413 1857-1862.
414 Fang, L., Zheng, M., Liu, G., Zhao, Y., Liu, W., Huang, L., and Guo, L., 2017.
415 Unexpected promotion of PCDD/F formation by enzyme-aided $Cl_2$ bleaching
416 in non-wood pulp and paper mill. Chemosphere 168, 523-528.
417 Garcia-Segura, S., Garrido, J. A., Rodríguez, R. M., Cabot, P. L., Centellas, F., Arias,
418 C., and Brillas, E., 2012. Mineralization of flumequine in acidic medium by
419 electro-Fenton and photoelectro-Fenton processes. Water Res. 46, 2067-2076.
420 Guo, X., Wan, J., Yu, X., and Lin, Y., 2016. Study on preparation of
421 $SnO_2$-$TiO_2$/Nano-graphite composite anode and electro-catalytic degradation
422 of ceftriaxone sodium. Chemosphere 164, 421-429.
423 Gupta, A., and Garg, A., 2018. Degradation of ciprofloxacin using Fenton's oxidation:
424 Effect of operating parameters, identification of oxidized by-products and
425 toxicity assessment. Chemosphere 193, 1181-1188.
426 He, Y., Wang, X., Huang, W., Chen, R., Zhang, W., Li, H., and Lin, H., 2018.
427 Hydrophobic networked $PbO_2$ electrode for electrochemical oxidation of
428 paracetamol drug and degradation mechanism kinetics. Chemosphere 193,
429 89-99.
430 Hermabessiere, L., Dehaut, A., Paul-Pont, I., Lacroix, C., Jezequel, R., Soudant, P.,
431 and Duflos, G., 2017. Occurrence and effects of plastic additives on marine
432 environments and organisms: A review. Chemosphere 182, 781-793.

433 Jiang, Y., Zhu, X., Li H., and Ni, J., 2010. Effect of nitro substituent on
434 electrochemical oxidation of phenols at boron-doped diamond anodes.
435 Chemosphere 78, 1093-1099.
436 Lai, P., Zhao, H., Zeng, M., and Ni J., 2009. Study on treatment of coking wastewater
437 by biofilm reactors combined with zero-valent iron process. J. Hazard. Mater.
438 162,1423-1429.
439 Li, H., Zhu, X. , Jiang, Y., and Ni, J., 2010. Comparative electrochemical degradation
440 of phthalic acid esters using boron-doped diamond and Pt anodes.
441 Chemosphere 80, 845-851.
442 Li, Y., Zhang, F.,. Liang, X, and Yediler, A., 2013. Chemical and toxicological
443 evaluation of an emerging pollutant (enrofloxacin) by catalytic wet air
444 oxidation and ozonation in aqueous solution. Chemosphere 90, 284-291.
445 Lindermeir, A., Horst, C., and Hoffmann, U., 2003. Ultrasound assisted
446 electrochemical oxidation of substituted toluenes. Ultrason. Sonochem. 10,
447 223-229.
448 Martínez-Huitle, C. A., Quiroz, M. A., Comninellis, C., Ferro, S., and Battisti, A. D.,
449 2004. Electrochemical incineration of chloranilic acid using Ti/$IrO_2$, Pb/$PbO_2$
450 and Si/BDD electrodes. Electrochim. Acta 50, 949-956.
451 Panizza, M., and Cerisola, G., 2004. Influence of anode material on the
452 electrochemical oxidation of 2-naphthol. Electrochim. Acta 49, 3221-3226.
453 Panizza, M., and Cerisola, G., 2005. Application of diamond electrodes to
454 electrochemical processes. Electrochim. Acta 51, 191-199.

455 Panizza, M., Kapalka, A., and Comninellis, C., 2008. Oxidation of organic pollutants
456 on BDD anodes using modulated current electrolysis. Electrochim. Acta 53,
457 2289-2295.
458 Panizza, M., Michaud, P. A., Cerisola, G., and Comninellis, C., 2001. Electrochemical
459 treatment of wastewaters containing organic pollutants on boron-doped
460 diamond electrodes: Prediction of specific energy consumption and required
461 electrode area. Electrochem. Commun. 3, 336-339.
462 Sathishkumar, K., Sathiyaraj, S., Parthipan, P., Akhil, A., Murugan, K., and Rajasekar,
463 A., 2017. Electrochemical decolorization of methyl red by $RuO_2$-$IrO_2$-$TiO_2$
464 electrode and biodegradation with Pseudomonas stutzeri MN1 and
465 Acinetobacter baumannii $MN_3$: An integrated approach. Chemosphere 183,
466 204-211.
467 Uyguner-Demirel, C. S., and Bekbolet, M., 2011. Significance of analytical
468 parameters for the understanding of natural organic matter in relation to
469 photocatalytic oxidation. Chemosphere 84, 1009-1031.
470 Vatistas, N., 2010. Adsorption layer and its characteristic to modulate the
471 electro-oxidation runway of organic species. J. Appl. Electrochem. 40,
472 1743-1750.
473 Wang, H., Qian, D., Xiao, X., He, B., Gao, S., Shi, H., Liao, L., and Deng, J., 2017.
474 Enantioselective determination of S-ornidazole by using carbon paste
475 electrode modified with boron-embedded conductive
476 copolymer-polysiloxane-based molecularly imprinted hybrid film.

Electrochim. Acta 246, 338-347.

Wee, S. Y., and Aris, A. Z., 2017. Ecological risk estimation of organophosphorus pesticides in riverine ecosystems. Chemosphere 188, 575-581.

Wei, L., Guo, S., Yan, G., Chen, C., and Jiang, X., 2010. Electrochemical pretreatment of heavy oil refinery wastewater using a three-dimensional electrode reactor. Electrochim. Acta 55, 8615-8620.

Wei, J., Zhu, X., andNi, J., 2011. Electrochemical oxidation of phenol at boron-doped diamond electrode in pulse current mode. Electrochim. Acta 56, 5310-5315.

Xing, X., Zhu, X., Li, H., Jiang, Y., and Ni, J., 2012. Electrochemical oxidation of nitrogen-heterocyclic compounds at boron-doped diamond electrode. Chemosphere 86, 368.

Yang, B., Shen, Z., Cheng, Z., and Ji, W., 2017. Total nitrogen removal, products and molecular characteristics of 14 N-containing compounds in supercritical water oxidation. Chemosphere 188, 642-649.

Yi, J., Zhu, X., Li, H., and Ni, J., 2010. Effect of nitro substituent on electrochemical oxidation of phenols at boron-doped diamond anodes. Chemosphere 78, 1093.

Zhao, G., Shen, S., Li, M., Wu, M., Cao, T., and Li, D., 2008. The mechanism and kinetics of ultrasound-enhanced electrochemical oxidation of phenol on boron-doped diamond and Pt electrodes. Chemosphere 73, 1407-1413.

Zhao, G., Zhang, Y., lei, Y., Lv, B., Gao, J., Zhang, Y., and Li. D., 2010. Fabrication and electrochemical treatment application of a novel lead dioxide anode with superhydrophobic surfaces, high oxygen evolution potential, and oxidation

capability. Environ. Sci. Technol. 44, 1754-1759.

Zhou, M., Liu, L., Jiao, Y., Wang, Q., and Tan, Q., 2011. Treatment of high-salinity reverse osmosis concentrate by electrochemical oxidation on BDD and DSA electrodes. Desalination 277, 201-206.

Zhu, X., and Ni, J., 2011. The improvement of boron-doped diamond anode system in electrochemical degradation of p-nitrophenol by zero-valent iron. Electrochim. Acta 56, 10371-10377.

Zhu, X., Ni, J., and Lai, P., 2009. Advanced treatment of biologically pretreated coking wastewater by electrochemical oxidation using boron-doped diamond electrodes. Water Res. 43, 4347-4355.

Zhu, X., Ni, J., Li, H., Jiang, Y., Xing, X., and Borthwick, A. G. L., 2010a. Effects of ultrasound on electrochemical oxidation mechanisms of *p*-substituted phenols at BDD and $PbO_2$ anodes. Electrochim. Acta 55, 5569-5575.

Zhu, X., Ni, J., Wei, J., and Chen, P., 2011a. Scale-up of B-doped diamond anode system for electrochemical oxidation of phenol simulated wastewater in batch mode. Electrochim. Acta 56, 9439-9447.

Zhu, X., Ni, J., Wei, J., Xing, X., Li, H., and Jiang, Y., 2010b. Scale-up of BDD anode system for electrochemical oxidation of phenol simulated wastewater in continuous mode. J. Hazard. Mater. 184, 493.

Zhu, X., Ni, J., Wei, J., Xuan, X., and Li, H., 2011b. Destination of organic pollutants during electrochemical oxidation of biologically-pretreated dye wastewater using boron-doped diamond anode. J. Hazard. Mater. 189, 127-133.

521 Zhu, X., Shi, S., Wei, J., Lv, F., Zhao, H., Kong, J., He, Q., and Ni, J., 2007.
522 Electrochemical oxidation characteristics of *p*-substituted phenols using a
523 boron-doped diamond electrode. Environ. Sci. Technol. 41, 6541.
524 Zhu, X., Tong, M., Shi, S., Zhao, H., and Ni. J., 2008. Essential explanation of the
525 strong mineralization performance of boron-doped diamond electrodes.
526 Environ. Sci. Technol. 42, 4914-4920.
527

528 **Table 1 Experimental range and levels of independent variables.**

| Independent factors | Factor | Range and levels | | | | |
|---|---|---|---|---|---|---|
| | $X_i$ | -2 | -1 | 0 | 1 | 2 |
| Initial current density ($mAcm^{-2}$) | $X_1$ | 7 | 9 | 11 | 13 | 15 |
| Flow rate ($mLmin^{-1}$) | $X_2$ | 100 | 150 | 200 | 250 | 300 |
| Electrolysis time (min) | $X_3$ | 48 | 96 | 144 | 192 | 240 |
| Exponential decay constant $k$ ($s^{-1}$) | $X_4$ | $6\times10^{-5}$ | $8\times10^{-5}$ | $1\times10^{-4}$ | $1.2\times10^{-4}$ | $1.4\times10^{-4}$ |

529

530 **Table 2 Design matrix in coded units and the experimental responses.**

| Runs | A | B | C | D | $D_{COD}$ (%) | $E_{sp}$ (kWh $kgCOD^{-1}$) |
|---|---|---|---|---|---|---|
| 1 | -1 | -1 | -1 | -1 | 30.48 | 18.23 |
| 2 | 1 | -1 | -1 | -1 | 24.04 | 23.58 |
| 3 | -1 | 1 | -1 | -1 | 32.45 | 18.97 |
| 4 | 1 | 1 | -1 | -1 | 44.62 | 21.95 |
| 5 | -1 | -1 | 1 | -1 | 50.38 | 18.75 |
| 6 | 1 | -1 | 1 | -1 | 67.31 | 23.18 |
| 7 | -1 | 1 | 1 | -1 | 55.66 | 18.41 |
| 8 | 1 | 1 | 1 | -1 | 71.15 | 17.24 |
| 9 | -1 | -1 | -1 | 1 | 31.78 | 17.25 |
| 10 | 1 | -1 | -1 | 1 | 35.33 | 24.92 |
| 11 | -1 | 1 | -1 | 1 | 33.33 | 16.30 |
| 12 | 1 | 1 | -1 | 1 | 39.22 | 22.28 |
| 13 | -1 | -1 | 1 | 1 | 52.9 | 17.99 |
| 14 | 1 | -1 | 1 | 1 | 59.46 | 22.27 |
| 15 | -1 | 1 | 1 | 1 | 56.48 | 16.69 |
| 16 | 1 | 1 | 1 | 1 | 61.97 | 20.22 |
| 17 | -2 | 0 | 0 | 0 | 39.37 | 16.69 |
| 18 | 2 | 0 | 0 | 0 | 60.00 | 23.44 |
| 19 | 0 | -2 | 0 | 0 | 41.51 | 23.91 |
| 20 | 0 | 2 | 0 | 0 | 55.28 | 18.52 |
| 21 | 0 | 0 | -2 | 0 | 21.62 | 19.34 |
| 22 | 0 | 0 | 2 | 0 | 71.03 | 19.22 |
| 23 | 0 | 0 | 0 | -2 | 59.83 | 18.35 |
| 24 | 0 | 0 | 0 | 2 | 48.18 | 17.10 |
| 25 | 0 | 0 | 0 | 0 | 51.46 | 19.43 |
| 26 | 0 | 0 | 0 | 0 | 51.36 | 18.23 |
| 27 | 0 | 0 | 0 | 0 | 49.55 | 18.72 |
| 28 | 0 | 0 | 0 | 0 | 50.02 | 19.23 |
| 29 | 0 | 0 | 0 | 0 | 52.4 | 18.69 |
| 30 | 0 | 0 | 0 | 0 | 52.4 | 18.85 |
| 31 | 0 | 0 | 0 | 0 | 49.53 | 19.55 |

531

532 **Figure Captions**

533 **Figure 1** Evolution of phenol concentration (A), COD concentration (B), the
534 difference between removal percentage of phenol and COD (C), and current
535 efficiency (D) as functions of electrolysis time at the BDD (■), $PbO_2$ (●) and $SnO_2$
536 (▲) anodes for the exponential decay current mode.

537 **Figure 2** Evolution of hydroxyl radicals concentration as function of electrolysis time
538 at BDD, $PbO_2$ and $SnO_2$ anodes (A), Utilization efficiency of hydroxyl radicals for
539 phenol oxidation at BDD, $PbO_2$ and $SnO_2$ anodes (B).

540 **Figure 3** Comparison between experimental (●) and predicted (■) results for $D_{COD}$
541 (A) and $E_{sp}$ (B), subplots (C) and (D) show the normalized residuals for $D_{COD}$ and $E_{sp}$.

542 **Figure 4** Contour plots of $D_{COD}$ in BDD anode system plotted according to: (A) initial
543 current density and flow rate, (B) initial current density and electrolysis time, (C) flow
544 rate and electrolysis time, (D) electrolysis time and exponential decay constant *k*.

545 **Figure 5** Contour plots of $E_{sp}$ in BDD anode system plotted according to: (A) initial
546 current density and flow rate, (B) initial current density and electrolysis time, (C) flow
547 rate and electrolysis time, (D) initial current density and exponential decay constant *k*.

Figure 1
Click here to download high resolution image

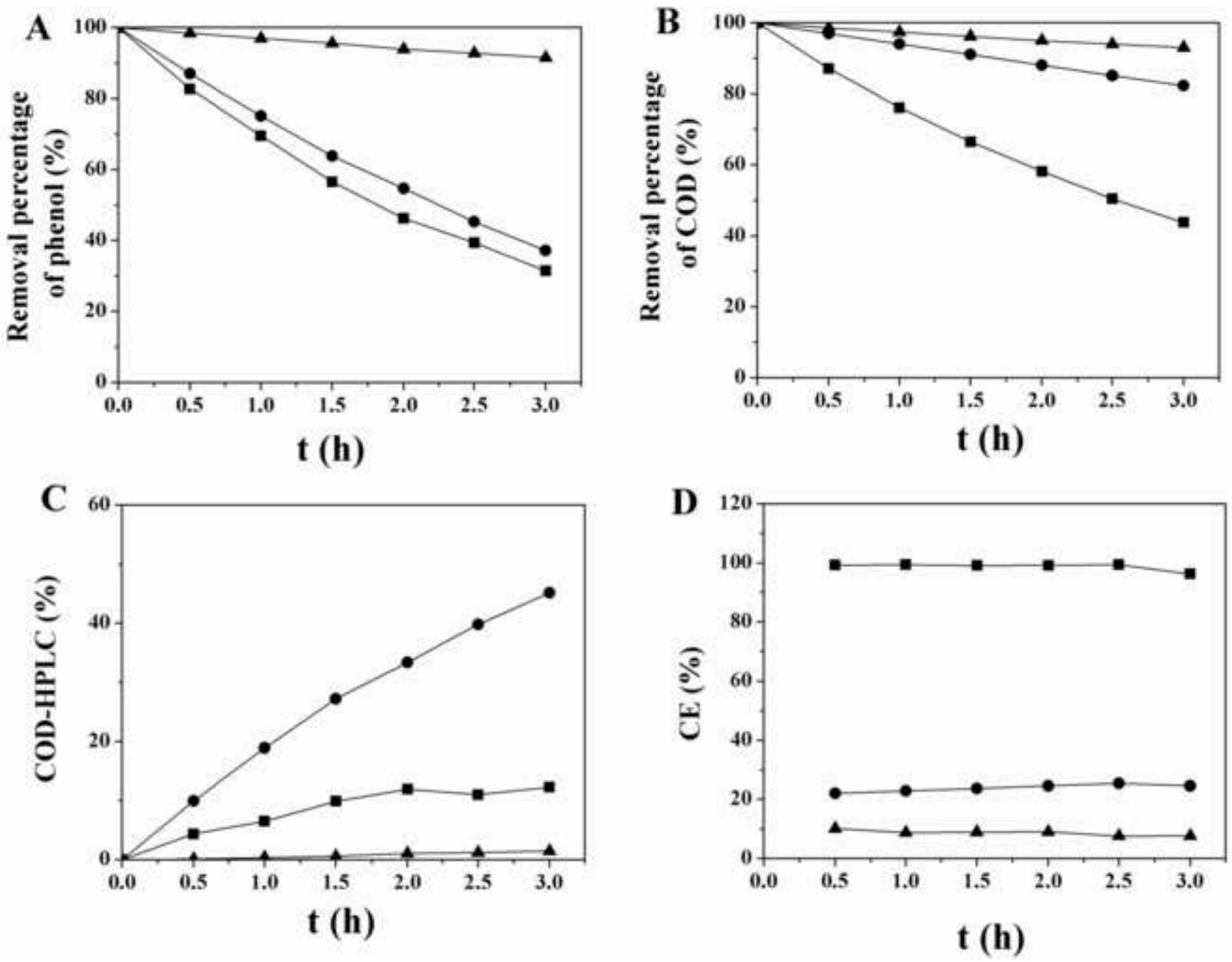

**Figure 2**

Click here to download high resolution image

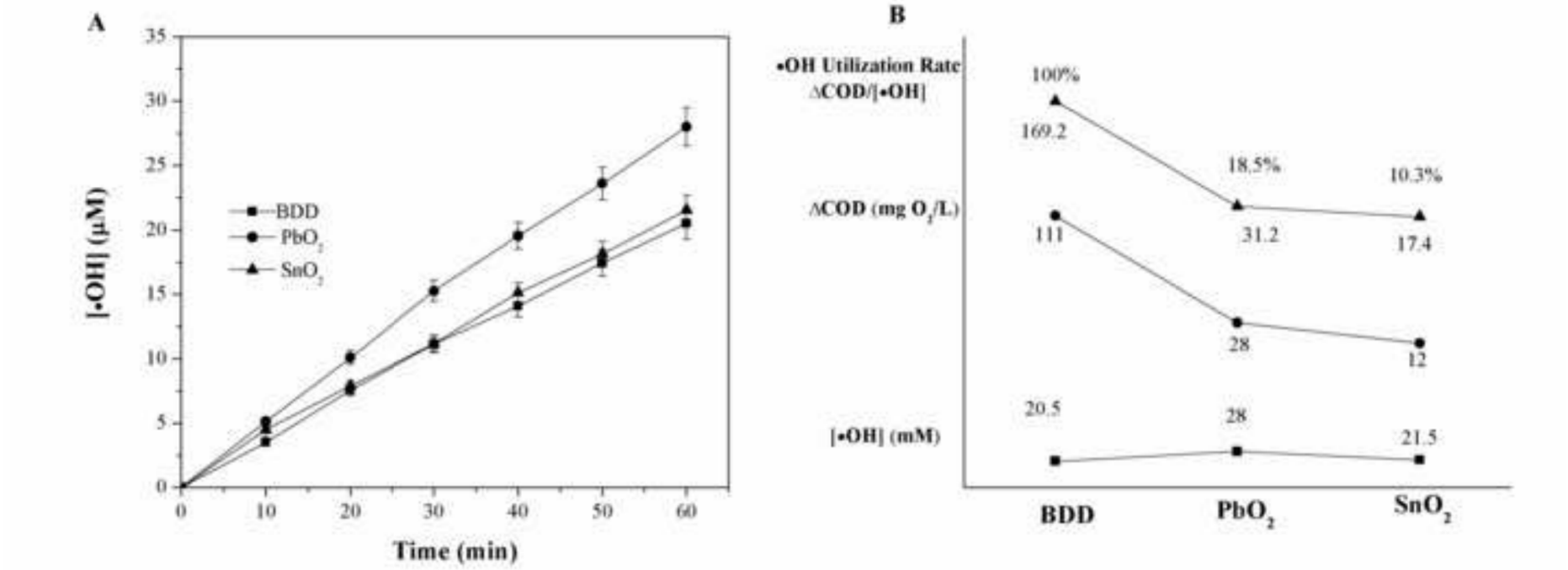

Figure 3
Click here to download high resolution image

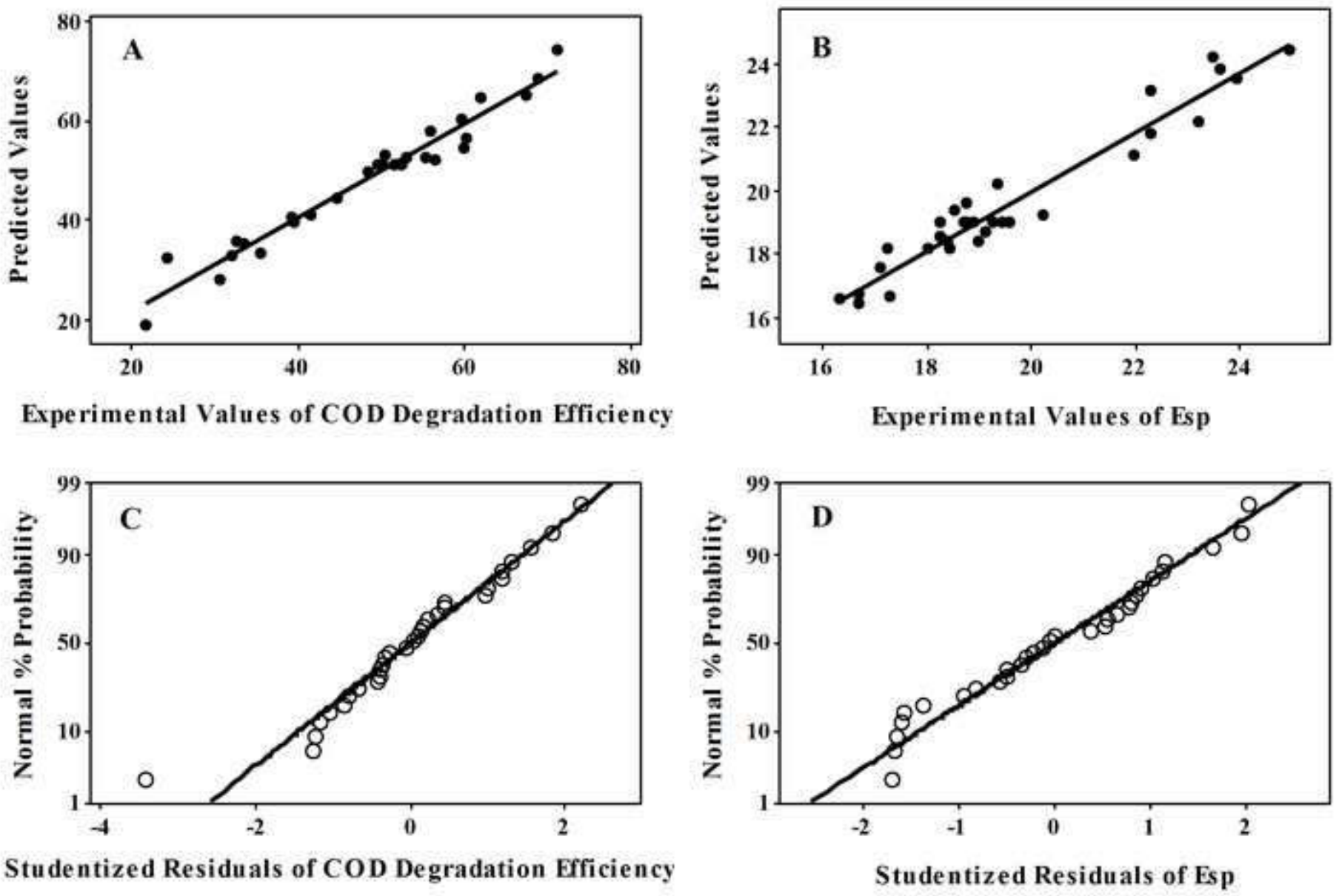

Figure 4
Click here to download high resolution image

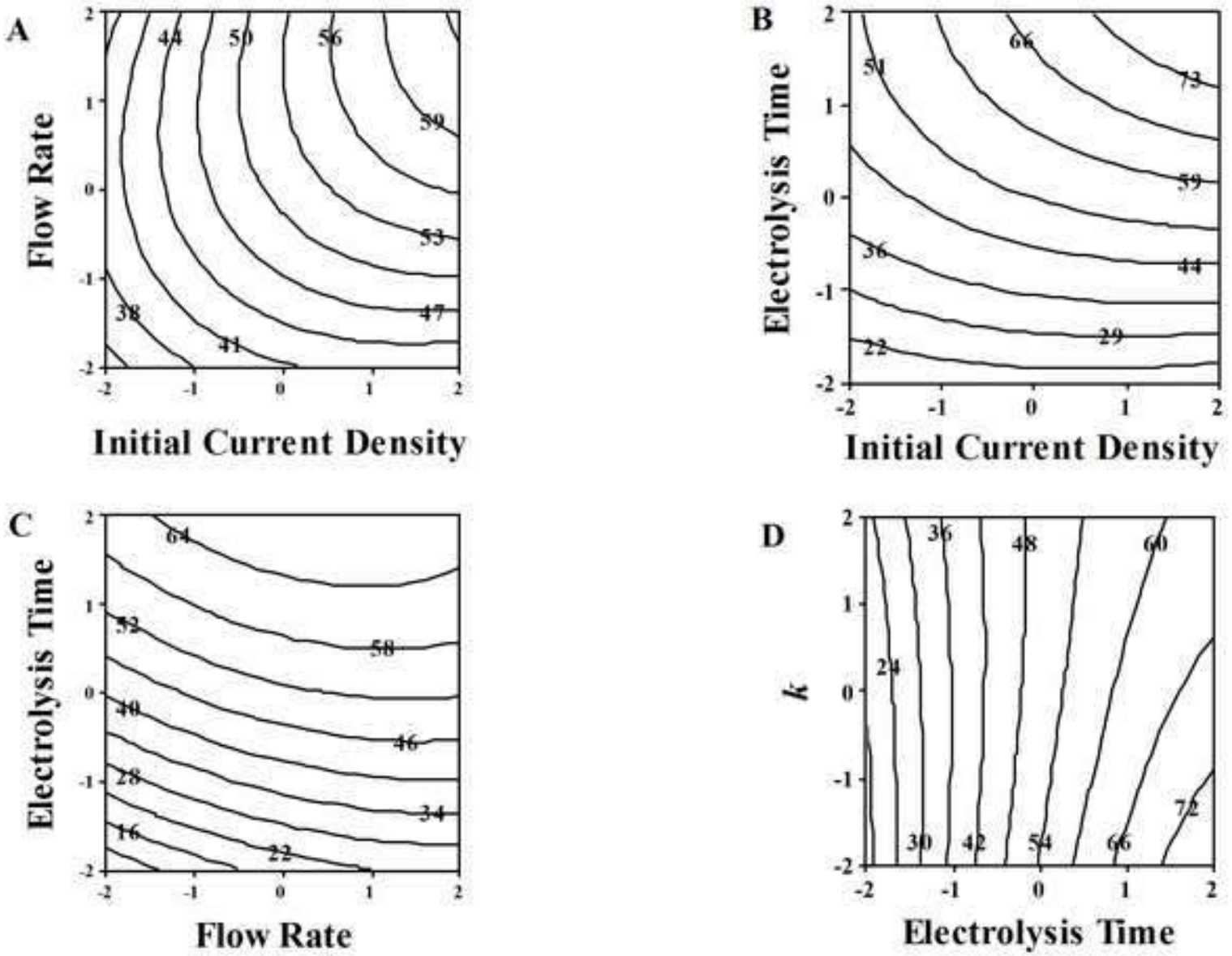

Figure 5
Click here to download high resolution image

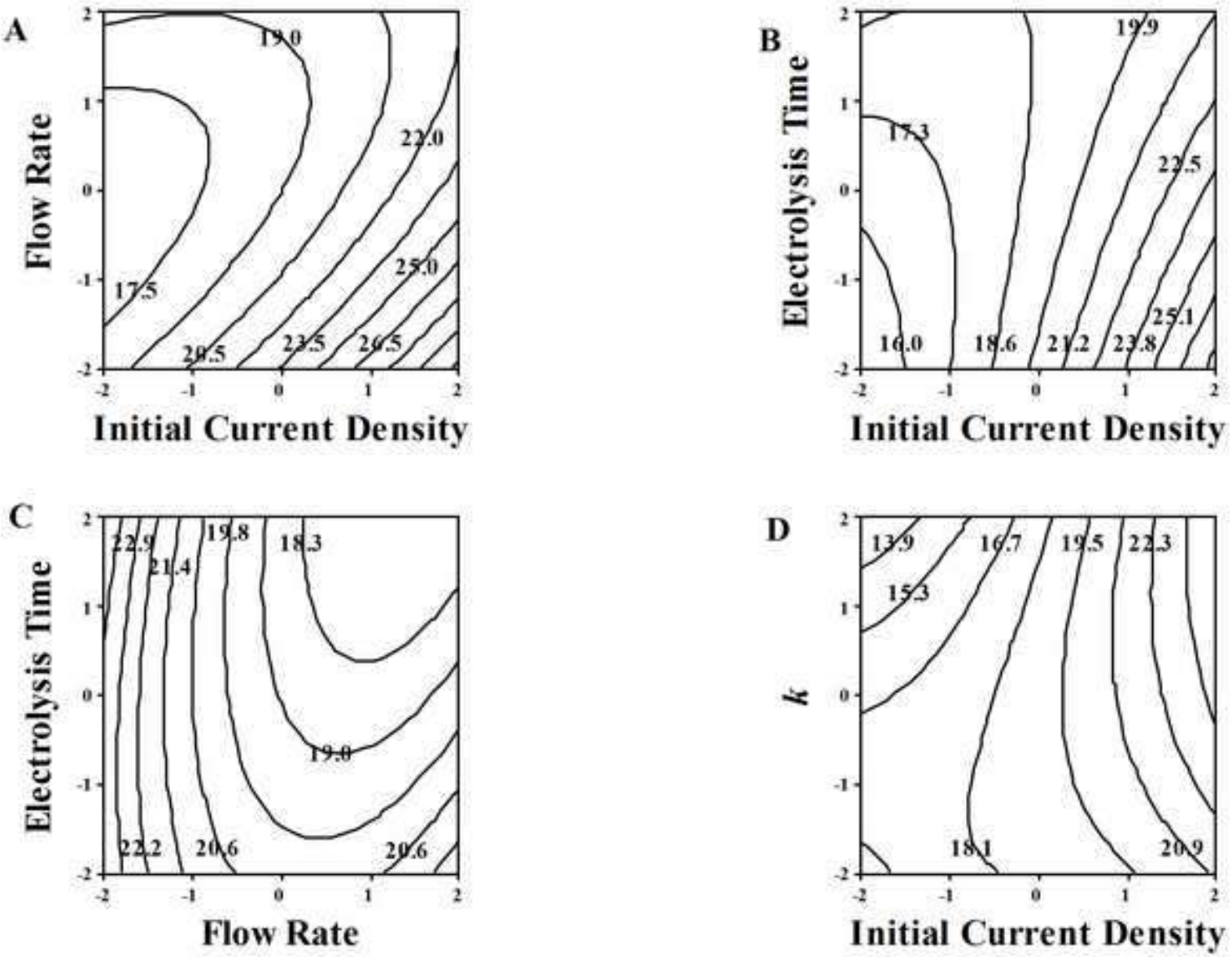

**Supplementary Material**

**Click here to download Supplementary Material: Supporting Information.docx**